Chemical Geology 507 (2019) 54–63

Contents lists available at ScienceDirect

Chemical Geology

journal homepage: www.elsevier.com/locate/chemgeo

Two episodes of sulfide mineralization at the Yuhuang-1 hydrothermal field on the Southwest Indian Ridge: Insight from Zn isotopes

Shili Liao[a,b], Chunhui Tao[a,b,*], Chuanwei Zhu[a,b,c], Huaiming Li[a,b], Xiaohu Li[a,b], Jin Liang[a,b], Weifang Yang[a,b], Yejian Wang[a,b]

[a] Second Institute of Oceanography, Ministry of Natural Resources, Hangzhou 310012, China
[b] Key Laboratory of Submarine Geosciences, State Oceanic Administration, Hangzhou 310012, China
[c] State Key Laboratory of Ore Deposit Geochemistry, Institute of Geochemistry, Chinese Academy of Sciences, Guiyang 550081, China

ARTICLE INFO

Editor: E. Böttcher Michael

Keywords:
Zn isotopes
Hydrothermal sulfide
Metallogeny
Yuhuang-1
Southwest Indian Ridge

ABSTRACT

The newly discovered Yuhuang-1 hydrothermal field (YHF) on the Southwest Indian Ridge primarily contains two different sulfide distribution areas: the southwest sulfide (SWS) and the northeast sulfide (NES) distribution areas. In this study, Zn isotope compositions and element ratios of Zn, Fe, Cu, and Cd in the surface sulfides were analyzed to characterize Zn isotopic fractionation, ore-forming conditions, and mineralization processes of the YHF. The results indicate that sulfide-rich samples in the YHF exhibit intensive Zn isotopic fractionation, with δ^{66}Zn values ranging from −0.43‰ to 1.24‰. These values are not only larger than those currently reported for seafloor sulfides but are also larger than the values reported for the deposits on land. Remarkably, the obtained δ^{66}Zn value (−0.43‰) is the lowest one observed in seafloor sulfides (−0.26‰–1.17‰), currently. A study of Zn isotope systematics revealed that Zn isotope variations of sulfide-rich samples in the YHF were controlled by the sphalerite and pyrite content; the study also revealed that early minerals are rich in light Zn isotopes, but later minerals are rich in heavy Zn isotopes. A comparative study of previous data on Zn isotopes shows that Zn isotope fractionations in the YHF are likely attributed to Rayleigh fractionation, caused by mineral precipitation and multiple generations of pyrite. Further, Zn/Cd ratios of sulfide-rich samples indicate that the ore-forming temperature of the silicified sulfide-rich samples in the SWS probably formed under lower temperatures as compared with the silicified sulfide-rich chimney in the NES. Furthermore, sulfur and Zn isotope compositions in the SWS are significantly different from those in sulfide-rich samples of the NES, which suggests pervasively different metallogenic conditions, further indicating that they are probably products of separate mineralization episodes.

1. Introduction

In nature, zinc (Zn) has five stable isotopes: ^{64}Zn (48.63%), ^{66}Zn (27.90%), ^{67}Zn (4.10%), ^{68}Zn (18.75%), and ^{70}Zn (0.62%) (Rosman, 1972). Several instrumentations can be used to analyze the Zn isotope compositions, but advanced technology such as a multicollector inductively coupled plasma mass spectrometer (MC-ICP-MS) enables high-precision analysis of Zn isotope compositions. MC-ICP-MS has long-term reproducibility of less than ± 0.07% for δ^{66}Zn measurements (Mason et al., 2004). Such advances have provided new opportunities for studying Zn cycling by detecting minor isotopic composition shifts in nature, which in turn allows the elucidation of the geological processes responsible for these fluctuations (e.g., Mason et al., 2005; Cloquet et al., 2006; Toutain et al., 2008; Zhu et al., 2018). Zinc isotopes have several advantages over traditional stable isotopes: the fractionation mechanisms of Zn isotopes are relatively simple, and they remain unaffected by redox potential because Zn exists only in the form of Zn or Zn^{2+} in nature (Kavner et al., 2008). Therefore, the mineralization and metallogenic processes can be traced in detail when combined with other geochemical indicators. In addition, Zn is a dominant ore-forming element in different types of ore deposits; thus, it could be directly used to determine the ore-forming elements' migration and enrichment processes in hydrothermal fluids with a wide range (White, 2014). Previous studies show the variability of Zn isotope compositions in different end-members on the Earth such as rocks (Maréchal et al., 2000; Chapman et al., 2006), marine sediments and

* Corresponding author at: Second Institute of Oceanography, Ministry of Natural Resources, No. 36 Baochu North Street, Xihu District, Hangzhou City, Zhejiang Province, China.
E-mail address: taochunhuimail@163.com (C. Tao).

https://doi.org/10.1016/j.chemgeo.2018.12.037
Received 18 April 2018; Received in revised form 18 December 2018; Accepted 28 December 2018
Available online 02 January 2019
0009-2541/

sulfides (Pichat et al., 2003; John et al., 2008), biological materials (Maréchal et al., 2000; Liu et al., 2017), seawater (Bermin et al., 2006), and ore deposits (Mason et al., 2005; Kelley et al., 2009; Gagnevin et al., 2012; Zhou et al., 2014a, 2014b, 2016; Wang et al., 2017c). Preliminary analyses in the aforementioned studies illustrated that the isotopic composition of Zn changed in various geological features, which seem to be triggered by 1) changes in geochemical conditions (Fujii et al., 2011; Pasava et al., 2014); 2) mixing of multiple Zn sources (Wilkinson et al., 2005); and 3) kinetic fractionation during mineral precipitation (Kelley et al., 2009; Gagnevin et al., 2012; Zhou et al., 2014a, 2014b). As regards ore deposit studies, Zn stable isotopes have been distinctly applied in the tracing of ore sources, mineral precipitation mechanisms, and ore genesis studies of different deposit types, such as the volcanogenic massive sulfide (VMS) deposits (Kelley et al., 2009), Mississippi Valley-type Pb−Zn deposits (MVT) (Gagnevin et al., 2012; Zhou et al., 2014a, 2014b, 2016), magmatic hydrothermal deposits (Wang et al., 2017c), volcanic hot springs (Toutain et al., 2008; Chen et al., 2014), and mid-oceanic ridge hydrothermal activities (John et al., 2008; Möller, 2012). Therefore, Zn isotopes are considered as powerful tracers that could be used to enhance different geochemical processes.

Sulfides on mid-ocean ridges are products of ongoing hydrothermal activities. Sulfides from slow and ultraslow-spreading ridges are crucial sulfide resources in modern seafloor hydrothermal systems, that contribute approximately 86% of the total mid-ocean ridge (MOR) sulfide resources (Hannington et al., 2011). Hydrothermal activities on such types of ridge systems exhibit a diversity of sulfide mineralization (German et al., 2010; Tao et al., 2011, 2014; Connelly et al., 2012; Baumberger et al., 2016). Thus far, limited research has been conducted on ultraslow-spreading ridges in hydrothermal systems based solely on surficial sulfide samples owing to limited investigation and sampling (Tao et al., 2012). Therefore, new approaches are required to constrain subsurface processes in seafloor hydrothermal systems. The variation of $\delta^{66}Zn$ in hydrothermal systems is used to trace seafloor hydrothermal processes, which play a vital role in promoting the study of the geochemistry of vent fluid and hydrothermal circulation. Hence, in this study, sulfide-rich samples from the Yuhuang-1 hydrothermal field (YHF) on the Southwest Indian Ridge (SWIR), a typical ultraslow-spreading ridge, were selected for Zn isotope analysis to reveal element migration progressions and physical and chemical conditions during mineralization processes. In addition, this study also provides new insights into the applications of Zn isotopes to study ancient VMS deposits.

2. Geological background

The SWIR extends approximately 8000 km between the African and Antarctic plates. It is defined as an ultraslow-spreading MOR, with a semi-spreading rate of approximately 0.7–0.9 cm/year (Dick et al., 2003). The SWIR is characterized by rugged topography with a series of north–south striking transform faults (Fig. 1a). Topographical and geophysical surveys revealed that the morphology, crustal thickness, mantle composition, and magma activities of the SWIR are significantly different along the ridge axis (Georgen et al., 2001; Sauter et al., 2009; Jian et al., 2017). Along the 49°E–52°E sections, previous investigations reported intensive hydrothermal activities with a hydrothermal site frequency of ~2.5 sites per 100 km, which is similar to that of the Mid-Atlantic Ridge at 36°N–38°N (Tao et al., 2012). The local magma supply and crustal permeability have been proposed as the primary controllers of the distribution of hydrothermal activities on this ridge (Tao et al., 2012). The YHF, discovered on the 21st cruise of the RV Dayangyihao in 2010 (Han et al., 2010), is located on the south rift wall of segment 29 of the SWIR. This segment exhibits asymmetric spreading features, with a volcanic axis developed in the rift valley. This field is about 7.5 km away from the ridge axis and has a water depth of 1400–1600 m (Han et al., 2010, 2015). The terrain, where the hydrothermal field is located, exhibits NEE-striking highland features about 1500 m above the rift valley bottom (Fig. 1b) and develops a series of NE–NWW-striking faults. As reported by the data of several cruises conducted by the China Ocean Mineral Resources Research and Development Association (COMRA), the eastern side of the YHF mainly contains calcareous sediments, whereas the western side primarily comprises basalt and basaltic breccia. Furthermore, serpentinite were collected by TV-grab during the 21st and 40th cruises, suggesting that the existence of outcrops of ultrabasic rocks.

Two different sulfide-distributed areas have been discovered in the YHF: the southwest sulfide area (SWS) and the northeast sulfide area (NES). Both areas have diameters of about 500 m and are located at a distance of approximately 600 m. Deep tow observation and sampling results suggest that the SWS surface primarily contains discontinuous distributed Zn-rich sulfides and silicified sulfide-rich samples that exhibit mound features. Recent drilling exposed that some parts of the SWS feature of Zn- and Cu-rich sulfides covered by ~50-cm-thick calcareous sediments. This feature implies the occurrence of ancient high-temperature hydrothermal activities. The NES surface primarily comprises discontinuously distributed sulfide accumulations and sulfide chimneys. These sulfide chimneys are distributed separately on the basalts without collapsed sulfide accumulations, which is similar to Zn-rich sulfide chimneys occurring on the East Pacific Rise (EPR; Paradis et al., 1988). No active hydrothermal vents have been discovered in the SWS, suggesting that hydrothermal activity has likely ceased. In terms of mineralization, the collected sulfide samples mainly contain pyrite, sphalerite, marcasite, chalcopyrite, and amorphous silicon with additional pyrrhotite in the NES.

3. Methods and materials

3.1. Sulfide-rich sample descriptions

Four sulfide-rich samples collected by TV-grab were selected for the Zn isotope analysis, including a Zn-rich massive sulfide, a Fe-rich massive sulfide with a siliceous crust, a silicified sulfide-rich sample from the SWS, and a sample from a silicified sulfide-rich chimney from the NES (Fig. 2). Moreover, we also measured the Zn isotope compositions of two basalt samples, which were collected from the same region.

Sulfide-rich samples in the SWS generally exhibit porous structures without obvious concentrated venting features, indicating that they were probably recovered from a sulfide-rich mound. The Zn-rich massive sulfide sample contains a pyrite crust and a sphalerite core with a small fluid conduit (Fig. 2a). The crust primary contains pyrite (60%–70%), amorphous silicon (10%–20%), sphalerite (5%–10%), and marcasite (< 5%), whereas the core mainly contains sphalerite (> 60%), amorphous silicon (15%–20%), and pyrite (5%) with minor chalcopyrite (< 5%), marcasite (< 5%), and isocubanite (< 5%). Sphalerite grains adjacent to the conduit exhibit coarse grain size up to 1 mm. Sphalerites have two generations that are replaced by chalcopyrite and pyrite (Fig. 3a). Pyrite replaces sphalerite or is replaced by sphalerite, suggesting two generations of pyrite. The pyritic massive sulfide with a siliceous crust mainly contains two layers with different mineralogies. The siliceous crust primarily comprises amorphous silicon (40%–50%), pyrite (20%–30%), marcasite (10%), and sphalerite (5%–10%), whereas its inner part mainly contains pyrite and marcasite (Fig. 2b), characterized by multiple generation features (Fig. 3b, c). Several fluid conduits surrounded by pyrite were observed, indicating that the bottom pyrite zone minerals formed later. The silicified sulfide-rich sample mainly contains a marcasite (60%–70%) and pyrite (30%–40%) core with a crust comprising amorphous silicon (70%–80%), minor pyrite (10%–15%), marcasite (5%–10%), and sphalerite (5%–10%) (Fig. 2c). The sphalerite was commonly replaced by pyrite that had intergrown with marcasite (Fig. 3d, e). These mineral assemblages suggest that the SWS experienced multiple ore-forming

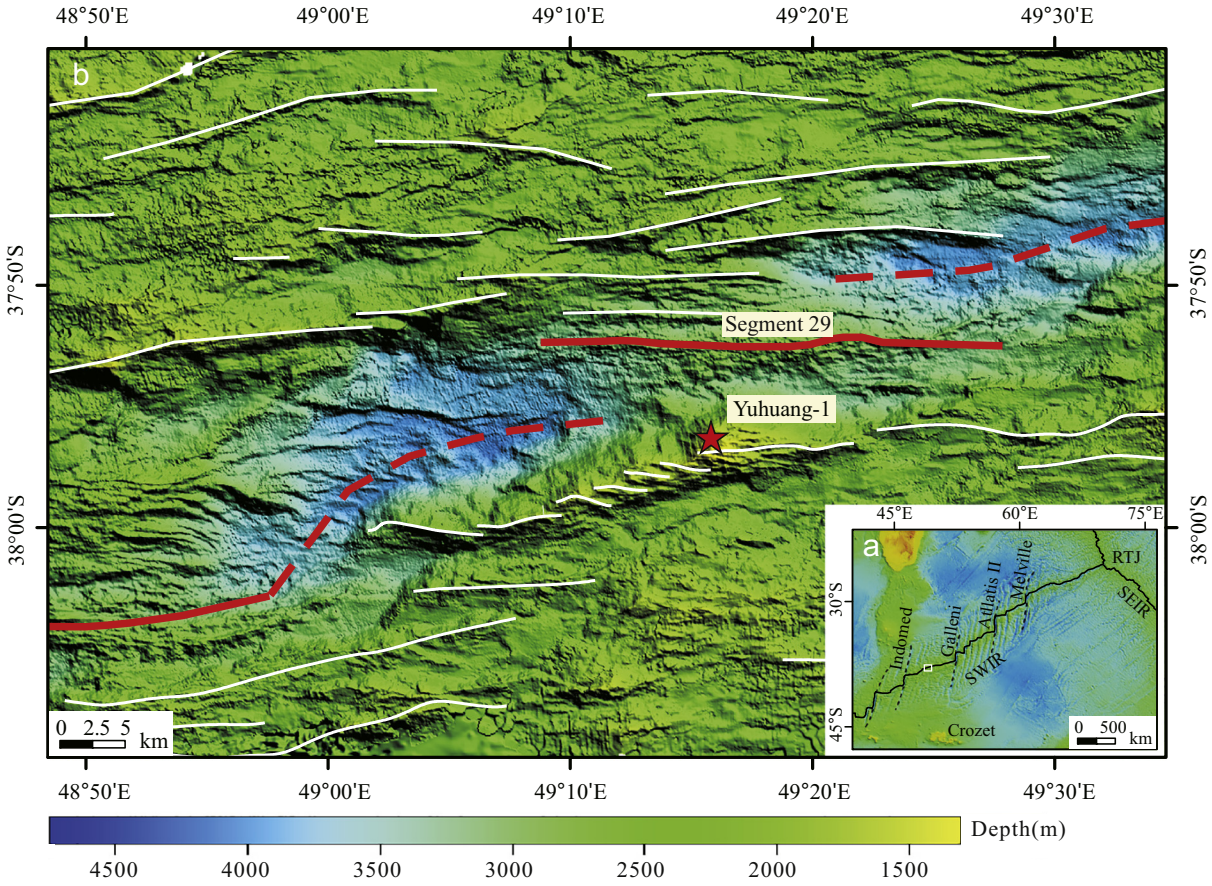

Fig. 1. (a) Geotectonic setting and (b) topography of the YHF. The red lines indicate the ridge axis and the white lines represent normal faults inferred from topography. The ridge segments and non-transform faults are based on Cannat et al. (1999) and Sauter et al. (2001). Data for (a) was taken from the General Bathymetric Chart of the Oceans (GEBCO), 2008; data for (b) was obtained using multibeam sonar data. (For interpretation of the references to colour in this figure legend, the reader is referred to the web version of this article.)

processes.

The silicified sulfide-rich sample of the NES was collected from a 1–2 m elevated chimney that lacked apparent fluid venting, which indicates that hydrothermal activity had ceased. The chimney grew directly on the basalt basement. The sample is porous and has multiple fluid conduits in which late-stage coarse sphalerite and opal are developed (Figs. 2d, 3f). The chimney mainly contains amorphous silicon (> 50%), sphalerite (20%–30%), pyrite (5%–10%), marcasite (5%), and minor pyrrhotite. Sphalerite grains usually replace pyrite and marcasite or are replaced by these minerals.

3.2. Microdrilling

On the scale of hand specimens, the sulfide-rich samples from the study area primarily contain sphalerite and pyrite with small grains of other sulfide minerals (e.g., chalcopyrite; Fig. 2 and 3). Separating pure sphalerite and pyrite from other minerals is challenging; therefore, this study employed a microdrilling system to obtain pure sphalerite and pyrite from the hand specimens for Zn isotope analysis. This method also provides a new approach to enhance the ability of understanding spatial Zn isotope variations in the hand specimens.

Microdrilling was performed using a microdrill system equipped with a 2-mm-diameter microdrill at the State Key Laboratory of Ore Deposit Geochemistry, Institute of Geochemistry, Chinese Academy of Sciences, China. The microdrilling targeted zones in the samples that were concentrated sphalerite and pyrite areas and were visually free of other minerals. However, obtaining pure sphalerite and pyrite without the presence of other minerals such as amorphous Si and chalcopyrite is difficult because micro-inclusions are unavoidable in most cases.

3.3. Zn separation

Before conducting the Zn isotope analysis, the microdrilling samples were chemically purified using a pre-cleaned 100–200 mesh AG MP-1M anion-exchange resin (Bio-Rad, USA) by following the detailed procedure provided by Zhu et al. (2018). Samples were individually transferred into Teflon digestion vials (Savilex; USA), and digested using 1 mL of concentrated HNO_3 and 0.1 mL of concentrated HF at 110 °C for approximately 24 h. After drying, the samples were dissolved into 10 mL of 1% HNO_3 (v/v%). Nearly 2 mL of a supernatant solution of the individual samples were transferred into a 15-mL polypropylene centrifuge tube for major and trace element analysis together with recovery-monitoring of Zn. Residual materials were evaporated to dryness and dissolved using 2 mL of 2 N HCl for Zn isotope separation. After adsorbing Zn onto the column, 10 mL of 2 N HCl and 12 mL of 0.3 N HCl were continuously passed through the columns. Ultimately, Zn was recovered using 12 mL of 0.012 N HCl. The remaining solution was dried at 110 °C and dissolved in 2 mL of 1% HNO_3 for Zn isotope measurement. Around 0.5 mL of the processed solution was transferred for Zn content measurement. The residuals (1.5 mL) were used for Zn isotope analysis. Finally, 99% of Zn was recovered by comparing the Zn content of unprocessed and processed samples.

3.4. Mass spectrometry measurements

Major and trace elements were determined via inductively coupled

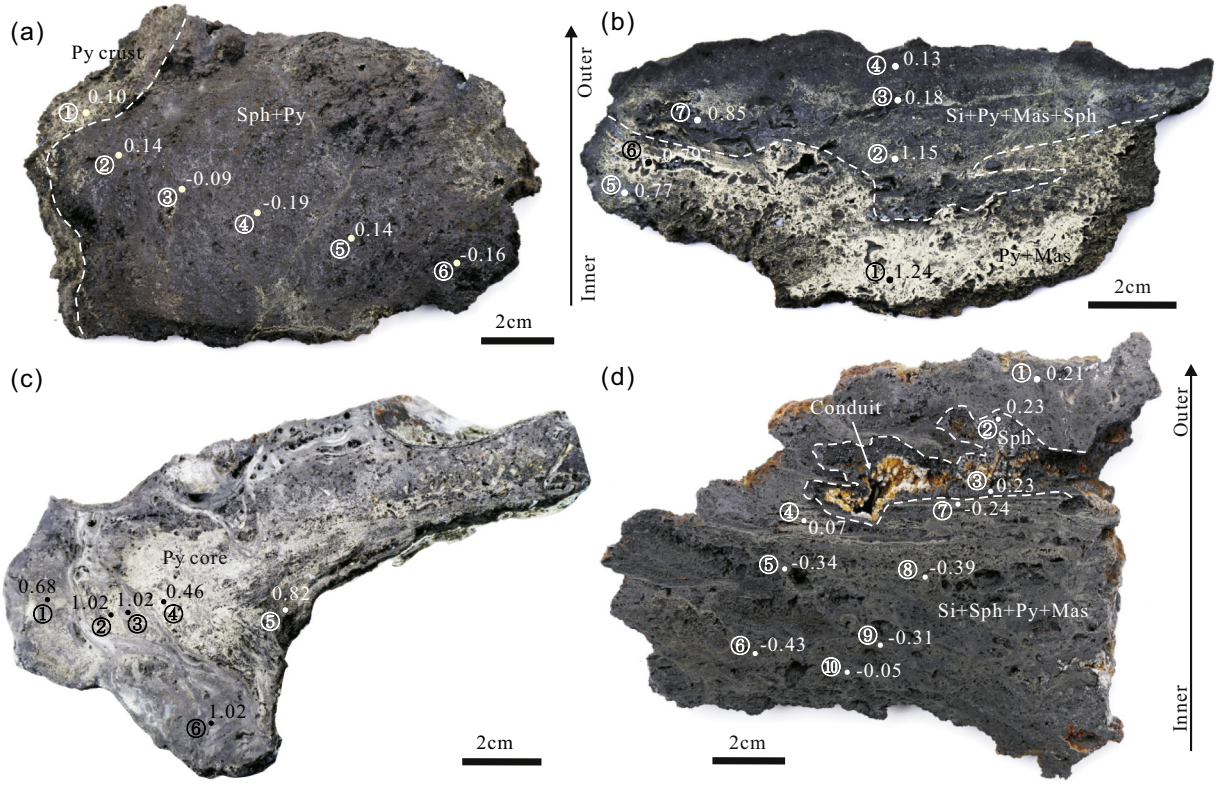

Fig. 2. Photos of sulfide-rich samples from the YHF for zinc isotope analysis. Samples (a)–(c) were collected from the SWS, whereas sample (d) was collected from the NES. (a) Zn-rich massive sulfide sample with a pyrite crust (34II-TVG22-2); (b) Fe-rich massive sulfide sample with a silicon crust (34II-TVG22-7); (c) silicified sulfide-rich sample with a pyrite core (34II-TVG22-4); (d) silicified sulfide-rich chimney with a fluid conduit (34II-TVG23-1) and sphalerites on the conduit walls that show coarse crystals. White and dark dots mark the microdrilling locations on the samples. Numbers with circles indicate microdrilling sample series for zinc isotope analysis corresponding to Table 1. Numbers adjacent to the circles indicate corresponding zinc isotope analysis results.

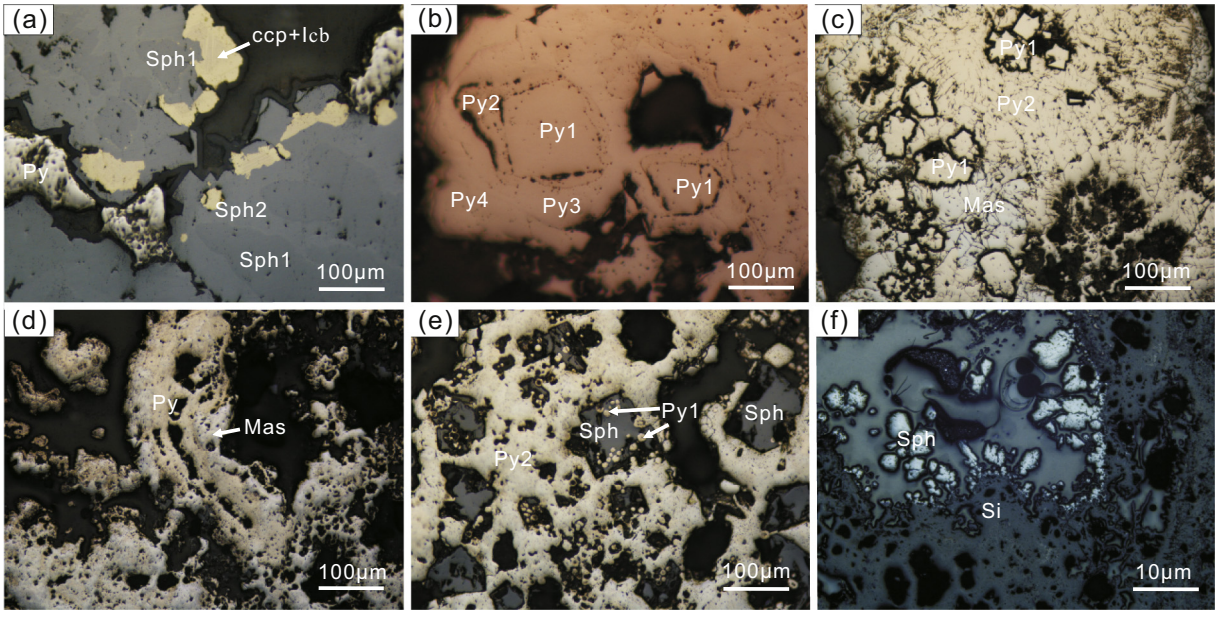

Fig. 3. Microscope photos of sulfide-rich samples in the YHF: (a) dark sphalerite (Sph1) replaced by light sphalerite (Sph2) and chalcopyrite (34II-TVG22-2); the chalcopyrite shows a grid structure with isocubanite; (b) Multiple generations of pyrite (34II-TVG22-7); (c) subhedral pyrite replaced by anhedral pyrite that intergrowth with marcasite (34II-TVG22-7); (d) anhedral pyrite intergrowth with marcasite (34II-TVG22-4); (e) fine grain euhedral pyrite recrystallized and replaced by sphalerite, and then replaced by anhedral pyrite(34II-TVG22-4); (f) sphalerite grains in the fluid conduit showing increasing diameters toward the conduit center (34II-TVG23-1). Mineral abbreviations: Ccp, chalcopyrite; Icb, isocubanite; Mas, marcasite; Py, pyrite; Sph, sphalerite; Si, amorphous silicon.

plasma optical emission spectrometry (ICP-OES) at the ALS Laboratory Group in Guangzhou, China. Two standards (ALSWAT01 and ALSWATx10, Inorganic Ventures, USA) were followed for determining major and trace elements with relative differences between replicates < 10%.

Zn isotope analyses were performed using a Neptune plus MC-ICP-MS instrument at the State Key Laboratory of Crust-Mantle Evolution and Mineralization, Nanjing University, China. Instrumental mass bias correction of Zn isotopes was adopted from Zhu et al. (2015) through a coupled method of sample-standard bracketing and Cu-doping. The Faraday cups were aligned to measure ^{63}Cu (L3), ^{64}Zn (L2), ^{65}Cu (L1), ^{66}Zn (center cup), ^{67}Zn (H1), ^{68}Zn (H2), and ^{70}Zn (H4) isotopes. Zn and Cu concentrated (ERM-AE633) samples and standards were diluted to 1.0 μg/g and 0.5 μg/g, respectively, using 1% HNO_3 (v/v). Subsequently, identical concentrations of both samples and standards were prepared within a 10% difference. Both samples and standards were analyzed at an uptake rate of ~100 μL/min and generally yielded a total Zn voltage of 30 V. All samples and standard solutions were run in three blocks of 15 cycles each. The nebulizer and spray chamber were washed with 5% HNO_3 (v/v) after each run until the voltage reached its original background level (~3 min). In this study, Zn isotope compositions were expressed in a standard delta notation of per mil units relative to the IRMM 3702a Zn solution during measurements. The Zn isotope compositions was shown as $\delta^{66}Zn = [(^{66}Zn/^{64}Zn)_{sample}/(^{66}Zn/^{64}Zn)_{IRM\text{-}3702a} - 1] \times 1000$.

During the Zn isotope analysis, samples were analyzed twice to calculate the analysis error. The CAGS-1 Zn standard solution was also used as an inner-laboratory secondary reference material, providing a long-term ($n = 6$) average $\delta^{66}Zn_{IRMM\ 3702}$ of −0.82‰ ± 0.05‰, which is consistent with previously reported values ($\delta^{66}Zn_{IRMM\ 3702}$ = −0.77‰ ± 0.10‰, Tang et al., 2016; $\delta^{66}Zn_{IRMM\ 3702}$ = −0.84‰ ± 0.03‰, Zhu et al., 2018). The Johnson Matthey (JMC)'s "Lyon solution" is used as an international Zn isotope composition standard. This study also reports Zn isotope data relative to the JMC standard using an equation expressed as $\delta^{66}Zn_{JMC} = \delta^{66}Zn_{IRMM\ 3702} + 0.29$ (Wang et al., 2017b).

4. Results

In this study, we reported Zn/Fe, Zn/Cu, and Zn/Cd ratios, which could be used to evaluate the mineral assemblages of the sulfide-rich samples (Table 1). The data show that sphalerite and pyrite are the two dominant minerals in the micro drilling samples (Table 1 and Fig. 3).

19 microdrilling samples of the specimens from the SWS exhibit δ^{66}Zn values ranging from −0.19‰ to ~1.24‰, with an average value of 0.53‰. The Zn isotope compositions of Zn-rich massive sulfide, Fe-rich massive sulfide, and silicified sulfide-rich samples are range from −0.19‰ to 0.14‰, 0.13‰ to 1.24‰, and 0.46‰ to 1.02‰, respectively. The Zn-rich massive sulfide exhibits lower δ^{66}Zn values than Fe-rich massive sulfide and silicified sulfide-rich samples (Fig. 4). In contrast, 10 microdrilling samples from the NES's silicified sulfide-rich chimney exhibit δ^{66}Zn values between −0.43‰ and 0.23‰, with an average value of −0.10‰. These values are significantly lower than the sulfide-rich samples from the SWS.

The two basalt samples exhibit δ^{66}Zn values of 0.23‰ and 0.25‰, which are consistent with the reported values of MOR basalts from different oceans (δ^{66}Zn = 0.25‰; Ben Othman et al., 2003; Wang et al., 2017b).

5. Discussion

5.1. Occurrence of Zn in sulfide-rich samples

Seafloor sulfides are an amalgamation of different minerals, such as chalcopyrite, isocubanite, marcasite, pyrrhotite, pyrite, and sphalerite. Among them, sphalerite is the predominant Zn-bearing mineral. Microscopic observations revealed that sulfide-rich samples from the YHF mainly contain pyrite and sphalerite with minor pyrrhotite, chalcopyrite, and isocubanite. Hence, we propose that the Zn content of the analyzed samples primarily originates from sphalerite. However, pyrite could be a container of Zn (Zhang et al., 2014; Wang et al., 2017a). Previous studies of in-situ analysis of seafloor pyrite reported high concentrations of Zn within pyrite (up to 15,000 μg/g; Keith et al., 2016), which most probably reflects micro-particle inclusions of sphalerite (Reich et al., 2013). Thus, the Zn isotope compositions of the high-Zn-content pyrites are representative of Zn isotope compositions. However, majority of the pyrite predominant samples exhibit low Zn concentration in the YHF, implying that Zn likely does not originate from sphalerite micro-particles in pyrite. Our reasoning for this conclusion is as follows.

First, microdrilling samples of the Fe-rich massive sulfide sample (34II-TVG22-7) have low Zn/Fe ratios and few sphalerite particles in the pyrite concentrated area, suggesting low Zn concentrations (Fig. 2b and Table 1). These results strongly suggest that Zn content in such types of samples (e.g., 34II-TVG22-7-1) is derived from the pyrite lattice (Bueker and Eyert, 1999). Further, previous electron probe micro-analyzer (EPMA) results (unpublished data) show that pyrite Zn/Fe ratios in the SWS and NES areas varied from 0.000 to 0.0113 (average 0.0015 ± 0.003 (2SD; $N = 24$)) and 0.0002 to 0.0217 (average 0.0014 ± 0.007 (2SD; $N = 10$)), respectively. Some samples exhibit a Zn/Fe ratio lower than the highest Zn/Fe ratio (0.0217) measured using EPMA. This result indicates that Zn constituents in some pyrite dominant samples, whose Zn/Fe ratio is < 0.03, emanated from pyrite rather than sphalerite micro-inclusions (e.g., 34II-TVG22-7-1; Table 1). Furthermore, Zn isotope compositions in sphalerite-dominant samples (Zn/Fe > 3; Fig. 5a) are relatively homogenous, ranging from −0.16‰ to 0.23‰. In contrast, samples predominantly containing pyrite (Zn/Fe < 0.03; Fig. 5a) exhibit large Zn isotope fractionation (−0.39‰ to 1.24‰). Thus, Zn contents in samples predominantly containing pyrite are not primarily sourced from sphalerite micro-particles; rather, they are caused by the substitution of Fe in pyrite. Consequently, the occurrence of Zn is generally controlled by sphalerite and pyrite.

5.2. Zinc isotope systematics

Zn-rich massive sulfides in the SWS exhibit δ^{66}Zn values (−0.19‰–0.14‰), which is significantly lower than that of iron-rich massive sulfide (0.13‰–1.24‰) and silicified sulfide-rich (0.46‰–1.02‰) samples. Micro observations revealed high content of amorphous silicon in the iron-rich massive sulfide and silicified sulfide-rich samples. The high content of amorphous silicon is likely a product of low-temperature hydrothermal activity in the late stage (Yee et al., 2003; Sun et al., 2015). Therefore, it could be deduced that, with sphalerite precipitation, early sphalerite is rich in light Zn isotopes, but later minerals are rich in heavy Zn isotopes. This is also confirmed by the negative relationship between δ^{66}Zn values and Zn/Fe ratios of different types of sulfides (Fig. 5a), suggesting that Zn isotope fractionation in the SWS was controlled by mineral precipitation at the hydrothermal field evolution scale. Similar characteristics have also been identified in sulfides of the EPR 9°N segment, where sulfides (Bio-9′) formed at high temperatures (383 °C) have high Zn/Fe ratios and low δ^{66}Zn values. Conversely, K-vent sulfides formed at low temperatures (203 °C) have low Zn/Fe ratios and high δ^{66}Zn values (Fig. 5; John et al., 2008).

Interestingly, the local δ^{66}Zn values of Zn-rich massive sulfide and silicified sulfide-rich samples in the SWS increase with increasing Zn/Fe and Zn/Cu ratios. On the contrary, in the Fe-rich massive sulfide sample, the local δ^{66}Zn values show negative relationships with the Zn/Fe and Zn/Cu ratios (Fig. 5a and b). This indicates that the Zn isotope compositions were controlled by the sphalerite content in the former and by pyrite content in the latter, further indicating that samples with heavy Zn isotope compositions are enriched in sphalerite and light Zn

Table 1
Zinc and sulfur isotope composition of the sulfide rich samples in the YHF.

Sample	Type	Series	Mineral	$\delta^{34}S_{CDT}$(‰)	$\delta^{66}Zn_{JMC}$(‰)	2SD	Zn/Cd	Zn/Cu	Zn/Fe
34II-TVG22-2	Zinc rich massive sulfide	1	Py + Sph	2.55	0.10	0.04	575.00	15.54	0.026
		2	Sph	0.75	0.14	0.03	1418.52	79.30	5.232
		3	Sph	0.49	−0.09	0.02	580.00	54.12	5.194
		4	Sph	0.80	−0.19	0.00	494.25	40.57	4.076
		5	Sph + Ccp	0.53	0.14	0.01	966.67	56.80	5.284
		6	Sph	0.47	−0.16	0.02	505.00	77.69	3.848
34II-TVG22-4	Silicified sulfide rich sample	1	Py + Si + Sph	1.04	0.68	0.02	3430.00	263.85	0.571
		2	Py + Sph	2.65	1.02	0.00		89.00	0.072
		3	Si + Py + Sph	0.83	1.02	0.00	3840.00	101.05	0.741
		4	Py + Si	0.69	0.46	0.01		6.21	0.050
		5	Py + Sph	−0.34	0.82	0.02	2610.00	42.79	0.229
		6	Si + Py	0.07	1.02	0.04		71.33	0.473
34II-TVG22-7	Iron-rich massive sulfide with a silicified crust	1	Py + Mas	−1.37	1.24	0.06		2.75	0.002
		2	Si + Py + Mas	0.13	1.15	0.03		3.00	0.005
		3	Si + Py + Mas	0.58	0.18	0.06		3.65	0.023
		4	Si + Py + Mas	−1.28	0.13	0.00		16.83	0.079
		5	Py + Mas	1.18	0.77	0.05		3.17	0.022
		6	Py + Mas	−1.09	0.79	0.02		5.00	0.005
		7	Py + Mas	1.25	0.85	0.00		2.43	0.007
34II-TVG23-1	Silicified sulfide rich chimney	1	Si		0.21	0.03		177.00	0.294
		2	Sph	3.75	0.23	0.02	1130.77	96.71	5.250
		3	Sph	4.46	0.23	0.09	1733.33	88.14	4.063
		4	Py + Sph	7.47	0.07	0.04		66.00	0.026
		5	Sph	4.52	−0.34	0.03			0.181
		6	Sph	5.45	−0.43	0.00	127.00	63.50	0.074
		7	Sph + py	7.25	−0.24	0.01		87.50	0.310
		8	Sph + py	4.14	−0.39	0.07			0.028
		9	Sph	7.07	−0.31	0.09			0.068
		10	Sph	7.11	−0.05	0.05			0.072
34II-TVG23-10	Basalt				0.25	0.02	972.73	1.18	0.001
34II-TVG21	Basalt				0.23	0.00	912.50	0.84	0.001

Note: Data of $\delta^{34}S_{CDT}$ are from Liao et al. (2018). Series are micro sampling numbers shown in Fig. 2. Mineral abbreviations are the same as Fig. 3.

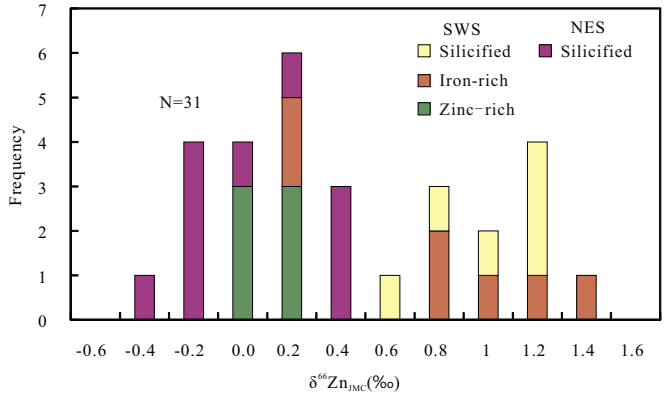

Fig. 4. Zinc isotope compositions frequencies of specimens from the YHF.

isotope compositions are enriched in chalcopyrite and pyrite. This conclusion was also confirmed by comparative studies of the EPR at 9°N (John et al., 2008), the Alexandrinka deposit (Mason et al., 2005), and the Red Dog deposit (Kelley et al., 2009). In addition, Fe-rich massive sulfide primarily contains pyrite with minor distributed sphalerite in the siliceous crust. Therefore, the Zn isotope compositions are probably interconnected to the precipitation of pyrite, which is clearly exhibited in Fig. 2b. The δ^{66}Zn values can be observed as gradually increasing from the edge to the core of the sulfide.

In the NES, δ^{66}Zn values of the silicified sulfide-rich chimney are significantly lower (−0.43–0.23‰) than those observed in the SWS. John et al. (2008) found that the variations of the vent fluid's Zn isotopes could be attributed to the precipitation of Zn-bearing minerals below the surface, and further suggested that the Zn isotopes may be a useful tool for evaluating the extent of Zn sulfide precipitation in different fluids. This result likely indicates the absence of intensive subsurface sulfide precipitation in the NES. Through deep tow observation results, it has been verified that sulfide chimneys in the NES grow directly on the basalt basement, whereas sulfide in the SWS displays sulfide mound features. In addition, the local δ^{66}Zn values increase with the increasing Zn/Fe ratios on the sulfide chimney scale (Fig. 5a). The δ^{66}Zn value of the early sulfide on the chimney edge is significantly lower than that of the late-stage fluid channel sulfide (Fig. 2d). Particularly, the two late-stage fluid channel samples with extremely high Zn/Fe ratios exhibit heavier Zn isotope compositions. This indicates that the Zn isotope compositions were controlled by sphalerite precipitation. However, the Zn/Cu ratios are generally stable with increasing δ^{66}Zn values, suggesting that δ^{66}Zn values are not affected by the chalcopyrite content. Therefore, it could be concluded that Zn isotope fractionation of the sulfide on the chimney is mainly controlled by mineral precipitation in the NES.

5.3. Intensive zinc isotope fractionation

The analysis results of sulfide-rich samples exhibit intensive Zn isotope fractionations in the YHF. The measured δ^{66}Zn value range (−0.43‰–1.24‰) is larger than that of the Lau basin (−0.19‰; Maréchal et al., 1999), the 9°N segment on the fast spreading EPR (−0.09‰–1.17‰; John et al., 2008), the Edmond and Kairei hydrothermal fields on the intermediate spreading Central Indian Ridge (−0.26‰–0.34‰; Wu et al., 2013), and the slow-spreading Southern Mid-Atlantic Ridge (13°S–15°S) (−0.14‰–0.38‰; Li et al., 2018). Our reported range is also significantly larger than the currently obtained δ^{66}Zn values of sulfides on the SWIR (−0.060‰ to 0.308‰; Wang et al., 2013). The value of −0.43‰ obtained from the NES is currently the lowest obtained value from seafloor sulfides (Fig. 6). Although sulfide-rich samples of the YHF were formed under medium–low temperatures, the range of δ^{66}Zn values was still larger than that currently obtained in magmatic hydrothermal deposits (Wang et al., 2017c),

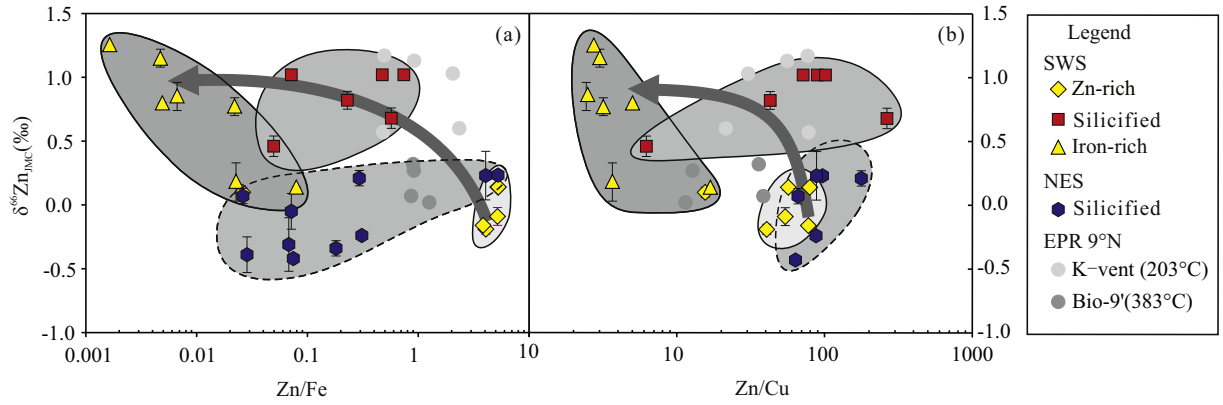

Fig. 5. Correlations between zinc isotope compositions and Zn/Fe (a), Zn/Cu(b) in the YHF. In the SWS, δ^{66}Zn values exhibit an increasing trending from Zn-rich massive sulfide to iron-rich massive sulfide. In addition, the local δ^{66}Zn values of Zn-rich massive sulfide and silicified sulfide-rich samples increase with Zn/Fe (a) and Zn/Cu(b) ratios increasing, while decrease in pyrite-rich massive sulfide. In the NES, the silicified sulfide-rich chimney exhibit δ^{66}Zn values increasing with Zn/Fe ratios increasing. Data of Bio-9′ and K-vent are from John et al. (2008).

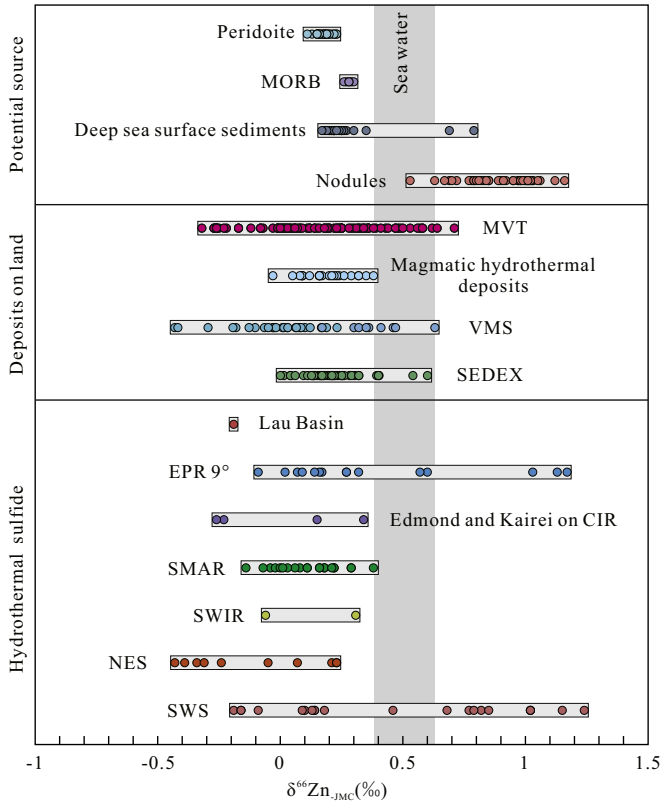

Fig. 6. Comparison of Zinc isotope compositions of the YHF with other HFs and mineralization types. Database: EPR 9°N (John et al., 2008); Lau Basin (Maréchal et al., 1999); Edmond and Kairei HFs in the Central Indian Ridge (Wu et al., 2013); Southern Mid-Atlantic Ridge (Li et al., 2018); Southwest Indian Ridge (Wang et al., 2013); hydrothermal Sb-Pb-An-Ag deposit (Duan et al., 2016; Wang et al., 2017c); Mississippi Valley-Type deposits (Wilkinson et al., 2005; Gagnevin et al., 2012; Zhou et al., 2014a, 2014b, 2016; He et al., 2016); VMS ore deposits (Mason et al., 2005; Kříbek et al., 2016); sedimentary exhalative deposits (Kelley et al., 2009; Gao et al., 2017); MOR basalts (Ben Othman et al., 2003; this study); peridotite (Huang et al., 2016; Wang et al., 2017b); nodules and deep sea surface sediments (Maréchal et al., 2000); and deep seawater ((Bermin et al., 2006; Zhao et al., 2014). Note: SWIR, and CIR data only plot minimum and maximum values because the references report only their distribution range.

Mississippi Valley-Type deposits (Wilkinson et al., 2005; Gagnevin et al., 2012; Zhou et al., 2014a, 2014b, 2016), sedimentary exhalative deposits (Kelley et al., 2009; Gao et al., 2017), and ancient VMS deposits (Mason et al., 2005; Kříbek et al., 2016). This indicates intensive Zn isotope fractionations in the hydrothermal field.

Zn isotope fractionation during mineralization is mainly caused by 1) Rayleigh fractionation due to mineral precipitation (Kelley et al., 2009; Gagnevin et al., 2012; Zhou et al., 2014a, 2014b, 2016); 2) fractionation between mineral assemblages (Mason et al., 2005; Wang and Zhu, 2010); and 3) mixing of separate derived fluids (Wilkinson et al., 2005).

The Zn isotopes of sulfide-rich samples in the YHF show a larger distribution range than deep seawater (0.53‰ ± 0.14‰; Bermin et al., 2006; Zhao et al., 2014), basalt (0.25‰; Table 1), deep sea carbonates (0.81‰–1.34‰; Pichat et al., 2003), deep sea clay and surface sediments 0.26‰–0.29‰ and 0.12‰–0.79‰ (Maréchal et al., 2000; Qi et al., 2012), manganese nodules (0.53‰–1.23‰; Maréchal et al., 2000; Little et al., 2014), and biogenic opal (0.8‰–1.5‰; Andersen et al., 2011) samples, respectively. Based upon published Zn isotope data of different end-members in such environments, mixing of fluids derived from the above origin could not result in such intensive fractionation during the formation of sulfide in the YHF.

We inferred that Zn isotope compositions of the YHF are mainly controlled by Rayleigh fractionation because of a perfect linear positive relationship existing between Zn/Cd ratios and δ^{66}Zn values (R = 0.95; Fig. 7). This suggests that the lower δ^{66}Zn-value sphalerite precipitated at higher temperature. Previous studies have shown that light Zn isotopes are preferred to enrich in solid phase minerals instead of solutions during sulfide precipitation (e.g., Mason et al., 2005; Wilkinson et al., 2005). Therefore, early-stage sulfide-rich samples have lower δ^{66}Zn values than late-stage samples. The characterization of mineral texture and ore structure indicates that early precipitated Zn-rich sulfide samples have lower δ^{66}Zn values than later massive pyrite sulfides, suggesting kinetic fractionation after the deposition of the sulfide-rich samples. This conclusion is consistent with previous studies that showed that hydrothermal fluids with low temperatures have the highest δ^{66}Zn values in seafloor hydrothermal systems (John et al., 2008). However, the Zn isotope signatures under equilibrium fractionation, where sphalerite precipitated at higher temperature, had higher δ^{66}Zn values (Fujii et al., 2011; Pasava et al., 2014). Therefore, Zn isotope fractionation in sulfide-rich samples from the YHF is not likely controlled by temperature. The relationship between fluid temperature and δ^{66}Zn may reflect that Cd is easier to substitute than Zn at high temperature.

Moreover, fractionation between mineral assemblages, caused by multiple hydrothermal activities, likely plays a vital role in the

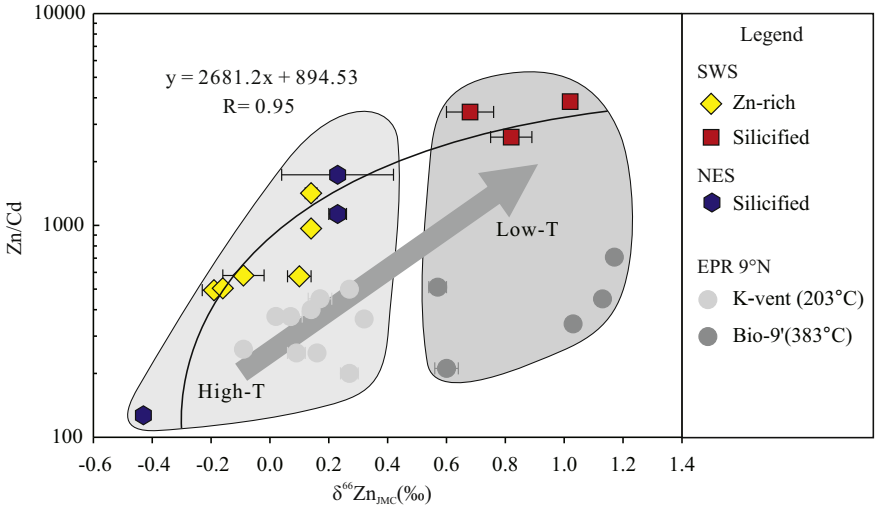

Fig. 7. Zn-rich massive sulfides formed under higher temperature show lower Zn/Cd ratio and δ^{66}Zn values than silicified sulfide-rich sample in the SWS. However, the silicified sulfide-rich chimney in the NES exhibits similar Zn/Cd ratio and δ^{66}Zn values as Zn-rich massive sulfide in the SWS, suggesting it was formed under higher temperatures than silicified sulfide-rich sample in the SWS. Data of EPR 9°N are from John et al. (2008).

formation of large Zn isotope fractions in the YHF. A microscopic study shows that pyrite is formed at all stages in the YHF, and sulfide-rich samples with low Zn/Fe ratios have significantly larger δ^{66}Zn values than those of mixed and pure sphalerite sulfide samples (Table 1). Zn is a minor element in pyrite and light Zn isotopes are more easily incorporated into pyrite structures. This is consistent with Zn isotope signatures between chalcopyrite, pyrite, and sphalerite, which shows that light Zn isotopes favor being accommodated into the pyrite and chalcopyrite lattice (Mason et al., 2005; Wang and Zhu, 2010). Zn isotope fractionations between pyrite and its parent fluids are larger than fractionations between sphalerite and its parent fluids. Therefore, the Zn isotope compositions increased among precipitated minerals and parent fluids during multiple pyrite precipitation stages. As a result, the late-stage pyrite exhibited significantly higher δ^{66}Zn values and led to a large distribution range of δ^{66}Zn values in pyrite-rich samples.

5.4. Ore-forming conditions of sulfide-rich samples

Wen et al. (2016) used the thermodynamic theory of the liquid–solid partitioning of Cd and Zn to conclude Cd distribution in sphalerite. To this end, they used various competing parameter influences, such as those of temperature, the presence of Cd complexes, salinity, and reduced sulfur and pH in hydrothermal fluids. As the temperature increases, more Cd isomorphously susbstitutes Zn in sphalerite. Thus, sphalerites formed under higher temperatures have lower Zn/Cd ratios than lower-temperature sphalerites (Schwartz, 2000; Wen et al., 2016; Zhu et al., 2016). Statistical analysis of mid-oceanic ridge sulfide Zn/Cd ratios shows that median Zn/Cd ratios gradually increase from the high-temperature chalcopyrite rich sulfide to the medium-temperature sphalerite–pyrite sulfide and low-temperature amorphous silicon–sphalerite–pyrite sulfide (Hannington et al., 2004). In the EPR 9°N, Cu-rich chimneys of the Bio 9′ vent formed at high temperature (383 °C) exhibit significantly lower Zn/Cd ratios than active Fe–Zn-rich chimneys and diffusers at the low-temperature K-vent (203 °C) (John et al., 2008; Fig. 7). Therefore, Zn/Cd ratios could be used to determine the formation temperature of seafloor sulfides.

In the SWS, the silicified sulfide-rich sample shows a significantly higher Zn/Cd ratio (average 3293.33) than that of the Zn-rich massive sulfide (average 756.57). This indicates that the latter formed at higher temperatures, which is consistent with the occurrence of isocubanite intergrowth with chalcopyrite in the Zn-rich sulfide. However, the silicified sulfide-rich chimney sample of the NES illustrates a Zn/Cd ratio (average 997.03) similar to that of the Zn-rich massive sulfide of the SWS, suggesting that the NES silicified chimney formed under higher temperature than the SWS silicified sulfide-rich sample. This corresponds to mineral assemblages that show silicified sulfide-rich samples and Fe-rich massive sulfide samples in the SWS to have a higher concentration of marcasite, which generally forms at temperatures < 240 °C with pH ≈ 3.9–5.0 (Murowchick and Barnes, 1986). In addition, previous studies have reported that Cd is strongly associated with Zn in terms of extraction efficiencies from basalt, transport, mixing, sulfide precipitation, and remobilization in seafloor hydrothermal systems (Metz and Trefry, 2000). High-reduced sulfur conditions favoring the formation of Cd-poor sphalerite, whereas low-reduced sulfur conditions favor the formation of Cd-rich sphalerite (Wen et al., 2016). Micro observations revealed that sulfide-rich samples in the NES contain pyrrhotite, suggesting that the ore-forming environment contains more reduced sulfur than the SWS. However, the Zn/Cd ratios of the Zn-rich massive sulfide samples from the SWS and the silicified sulfide-rich chimney samples from the NES are very close to those of the two basalts in the study area (Zn/Cd = 973, 913), whereas the silicified sulfide-rich sample from the SWS shows apparently higher Zn/Cd ratios, suggesting that the temperature likely has a more critical role in affecting Cd content in the sphalerite of the YHF. Therefore, the higher Zn/Cd ratios of the silicified sulfide-rich sample from the SWS could evidence a lower ore-forming temperature than that of the NES silicified chimney.

5.5. Two episodes of mineralization

Sulfide-rich samples of the SWS and NES have comparatively significant variations of Zn and S isotopic compositions, which indicate considerably different mineralization processes. The silicified sulfide-rich sample of the SWS had higher δ^{66}Zn values (0.46‰–1.02‰) than the Zn-rich massive sulfide sample (−0.19‰–0.14‰), suggested that it was formed at the late stage. However, the Zn isotope composition of the silicified sulfide-rich sample is distinctly higher than that of the silicified sulfide-rich chimney in the NES (−0.43‰–0.23‰); this indicates that the latter lacked a subsurface sulfide precipitation zone (John et al., 2008). In addition, the Zn/Cd ratios of the silicified sulfide-rich chimney and additional occurrence of pyrrhotite in the NES indicate that the ore-forming fluid in the NES probably had a higher temperature than that in the SWS. Furthermore, the SWS sulfide-rich samples are characterized by mound-like accumulation with a relatively closed metallogenic environment. Subsequently, the mixture of ore-forming fluid and seawater was relatively weak and fluid cooling was relatively slow (Tivey et al., 1995; Petersen et al., 2000). In contrast, the silicified sulfide-rich samples in the NES are isolated on the basalt basement, and mineralization conditions were relatively open

with a more rapid cooling process and sufficient seawater mixture (Paradis et al., 1988). This is evidenced by the sulfur isotopic composition of sulfide in the SWS being relatively concentrated and characterized by its proximity to basalt and bacteria-derived sulfur (−1.37‰–2.65‰); whereas silicified sulfide-rich chimneys in the NES are characterized by significantly heavier sulfur isotopic compositions (3.75‰–8.73‰; Liao et al., 2018). Previous studies suggested that the heavier sulfur isotopic composition of mid-oceanic ridge sulfides can only be explained by seawater reacting within the feeder zones immediately underlying seafloor deposits, which is possibly combined with additional sulfate reductions within sulfide structures (Janecky and Shanks, 1988). This indicates that the NES zone fluid undergoes mixing with seawater and reduction before venting from the seafloor. If sulfide-rich samples in the SWS and NES were formed in the same mineralization episode, then the SWS sulfide-rich samples should exhibit a tendency toward heavy-Zn isotope enrichment. Furthermore, sulfide-rich samples in the NES contained additional pyrrhotite as compared with the SWS sulfide-rich samples, suggesting prior formation in a relatively reduced environment (Kawasumi and Chiba, 2017). Therefore, it could be concluded that the sulfide-rich samples of the SWS and NES are likely products of different mineralization episodes.

6. Conclusion

(1) The sulfide mineralization processes of the YHF exhibit intensive Zn isotope fractionation features, with δ^{66}Zn values ranging between −0.43‰–1.24‰, which is not only larger than currently obtained seafloor sulfide data but also larger than the values obtained from deposits on the land. The Zn isotope fractionation was likely related to Rayleigh fractionation that was trigged by mineral precipitation and affected by mineral assemblages. The wide range of δ^{66}Zn values can be attributed to multiple generations of pyrite precipitation.

(2) The Zn/Cd ratios of sulfides indicate that the ore-forming temperature of Zn-rich massive sulfides in the SWS is higher than that of the silicified sulfide-rich samples, whereas the silicified sulfide chimney in the NES had a higher formation temperature than that observed in the SWS. The sulfide Zn/Cd ratios show a positive correlation with δ^{66}Zn values, which could be attributed to a decrease in temperature during mineralization.

(3) Sulfide-rich samples in the SWS and NES are likely formed during different mineralization episodes. Sulfide-rich samples in the NES are probably formed under higher temperatures and a more reduced environment, whereas a subsurface sulfide precipitation zone was probably lacking.

Acknowledgments

This research was funded by the National Key Research and Development Program of China (2018YFC0309902, 2017YFC0306603), Central Public-Interest Scientific Institution Basal Research Fund (JG1606), Natural Science Foundation of Zhejiang Province (LQ19D060002), Technology Upgrading and Scientific Applications of the 4500m Depth Rated “Qianlong II” AUV (2017YFC0306800), and China Ocean Mineral Resources R & D Association Project (DY135-S1-1-01 and 02). We would like to thank the captains and crews of the DY125-34 cruise on R/V DayangYihao, who contributed to the success of this project. Special thanks to Professor Chuanwan Dong for helping us improve the original draft, Dr. Zhiyong Zhu for helping us processing the analysis, and Dr. Zahid Hussain for helping us to polish the language. We are also grateful for the valuable comments and suggestions from two anonymous reviewers.

References

Andersen, M.B., Vance, D., Archer, C., Anderson, R.F., Ellwood, M.J., Allen, C.S., 2011. The Zn abundance and isotopic composition of diatom frustules, a proxy for Zn availability in ocean surface seawater. Earth Planet. Sci. Lett. 301 (1–2), 137–145.
Baumberger, T., Früh-Green, G.L., Thorseth, I.H., Lilley, M.D., Hamelin, C., Bernasconi, S.M., Okland, I.E., Pedersen, R.B., 2016. Fluid composition of the sediment-influenced Loki's Castle vent field at the ultra-slow spreading Arctic Mid-Ocean Ridge. Geochim. Cosmochim. Acta 187, 156–178.
Ben Othman, D., Luck, J.M., Tchalikian, A., Albarède, F., 2003. Cu-Zn isotope systematics in terrestrial basalts. Geophys. Res. Abstr. 1 (5), 9669.
Bermin, J., Vance, D., Archer, C., Statham, P.J., 2006. The determination of the isotopic composition of Cu and Zn in seawater. Chem. Geol. 226 (3–4), 280–297.
Bueker, Fiechter, Eyert, Tributsch, 1999. Photoelectrochemistry of highly Zn-doped pyrite as compared with isostructural FeS2. J. Electrochem. Soc. 30 (18), 261–265.
Cannat, M., Rommevaux-Jestin, C., Sauter, D., Deplus, C., Mendel, V., 1999. Formation of the axial relief at the very slow spreading Southwest Indian Ridge (49° to 69°E). J. Geophys. Res.-Atmos. 104 (B10), 22825–22843.
Chapman, J.B., Mason, T.F., Weiss, D.J., Coles, B.J., Wilkinson, J.J., 2006. Chemical separation and isotopic variations of Cu and Zn from five geological reference materials. Geostand. Geoanal. Res. 30 (1), 5–16.
Chen, J.B., Gaillardet, J., Dessert, C., Villemant, B., Louvat, P., Crispi, O., Birck, J., Wang, Y.N., 2014. Zn isotope compositions of the thermal spring waters of La Soufrière volcano, Guadeloupe Island. Geochim. Cosmochim. Acta 127 (02), 67–82.
Cloquet, C., Carignan, J., Libourel, G., 2006. Isotopic composition of Zn and Pb atmospheric depositions in an urban/periurban area of northeastern France. Environ. Sci. Technol. 40 (21), 6594–6600.
Connelly, D.P., Copley, J.T., Murton, B.J., Stansfield, K., Tyler, P.A., German, C.R., Van Dover, C.L., Amon, D., Furlong, M., Grindlay, N., 2012. Hydrothermal vent fields and chemosynthetic biota on the world's deepest seafloor spreading centre. Nat. Commun. 3, 620–628.
Dick, H.J., Lin, J., Schouten, H., 2003. An ultraslow-spreading class of ocean ridge. Nature 426 (6965), 405–412.
Duan, J.L., Tang, J.X., Lin, B., 2016. Zinc and lead isotope signatures of the Zhaxikang Pb Zn deposit, South Tibet: Implications for the source of the ore-forming metals. Ore Geol. Rev. 78, 58–68.
Fujii, T., Moynier, F., Pons, M., Albarède, F., 2011. The origin of Zn isotope fractionation in sulfides. Geochim. Cosmochim. Acta 75 (23), 7632–7643.
Gagnevin, D., Boyce, A.J., Barrie, C.D., Menuge, J.F., Blakeman, R.J., 2012. Zn, Fe and S isotope fractionation in a large hydrothermal system. Geochim. Cosmochim. Acta 88, 183–198.
Gao, Z.F., Zhu, X.K., Sun, J., Luo, Z.H., Bao, C., Tang, C., Ma, J.X., 2017. Spatial evolution of Zn-Fe-Pb isotopes of sphalerite within a single ore body: a case study from the Dongshengmiao ore deposit, Inner Mongolia, China. Mineral. Deposita 15, 1–11.
Georgen, J.E., Lin, J., Dick, H.J.B., 2001. Evidence from gravity anomalies for interactions of the Marion and Bouvet hotspots with the Southwest Indian Ridge: Effects of transform offsets. Earth Planet. Sci. Lett. 187 (3–4), 283–300.
German, C.R., Bowen, A., Coleman, M.L., Honig, D.L., Huber, J.A., Jakuba, M.V., Kinsey, J.C., Kurz, M.D., Leroy, S., Mcdermott, J.M., 2010. Diverse styles of submarine venting on the ultraslow spreading Mid-Cayman Rise. Proc. Natl. Acad. Sci. 107 (32), 14020–14025.
Han, X.Q., Wu, G.H., Cui, R., Qiu, Z.Y., Deng, X.M., Wang, Y., Dy, S.P.O., Leg, C., 2010. Discovery of a Hydrothermal Sulfide Deposit on the Southwest Indian Ridge at 49.2°E. American Geophysical Union (Fall Meeting, abstract#S21C-S1531C).
Han, X.Q., Wang, Y.J., Qiu, Z.Y., Liu, Y., Qiu, B.B., 2015. Discovery and mineralization features of the Yuhuang-1 hydrothermal field on Southwest Indian Ridge. Acta Mineral. Sin. 35 (S1), 1141–1142 (In Chinese with English abstract).
Hannington, M.D., Petersen, S., Herzig, P.M., Jonasson, I.R., 2004. A Global Database of Seafloor Hydrothermal Systems, Including a Digital Database of Geochemical Analyses of Sulfides Geological Survey of Canada Open File 4598.
Hannington, M., Jamieson, J., Monecke, T., Petersen, S., Beaulieu, S., 2011. The abundance of seafloor massive sulfide deposits. Geology 39 (12), 1155–1158.
He, C.Z., Xiao, C.Y., Wen, H.J., Zhou, T., Zhu, C.W., Fan, H.F., 2016. Zn-S isotopic compositions of the Tianbaoshan carbonate-hosted Pb-Zn deposit in Sichuan, China: Implications for source of ore components. Acta Petrol. Sin. 32 (11), 3394–3406 (In Chinese with English abstract).
Huang, J., Liu, S.A., Gao, Y., Xiao, Y., Chen, S., 2016. Copper and zinc isotope systematics of altered oceanic crust at IODP Site 1256 in the eastern equatorial Pacific. J. Geophys. Res. Solid Earth 121 (10), 7086–7100.
Janecky, D.R., Shanks, W.C.I., 1988. Computational modeling of chemical and sulfur isotopic reaction processes in seafloor hydrothermal systems: chimneys, massive sulfides, and subjacent alteration zones. Can. Mineral. 26, 805–825.
Jian, H.C., Chen, Y.J., Singh, S.C., Li, J.B., Zhao, M.H., Ruan, A.G., Qiu, X.L., 2017. Seismic structure and magmatic construction of crust at the ultraslow-spreading Southwest Indian Ridge at 50°28′E. J. Geophys. Res. Solid Earth 122 (1), 18–42.
John, S.G., Rouxel, O.J., Craddock, P.R., Engwall, A.M., Boyle, E.A., 2008. Zinc stable isotopes in seafloor hydrothermal vent fluids and chimneys. Earth Planet. Sci. Lett. 269 (1–2), 17–28.
Kavner, A., John, S.G., Sass, S., Boyle, E.A., 2008. Redox-driven stable isotope fractionation in transition metals: application to Zn electroplating. Geochim. Cosmochim. Acta 72 (7), 1731–1741.
Kawasumi, S., Chiba, H., 2017. Redox state of seafloor hydrothermal fluids and its effect on sulfide mineralization. Chem. Geol. 451, 25–37.
Keith, M., Haeckel, F., Haase, K.M., Schwarz-Schampera, U., Klemd, R., 2016. Trace element systematics of pyrite from submarine hydrothermal vents. Ore Geol. Rev. 72

(1), 728–745.
Kelley, K.D., Wilkinson, J.J., Chapman, J.B., Crowther, H.L., Weiss, D.J., 2009. Zinc isotopes in sphalerite from base metal deposits in the Red Dog district, northern Alaska. Econ. Geol. 104 (6), 767–773.
Kříbek, B., Zachariáš, J., Knésl, I., Míková, J., Mihaljevič, M., Veselovský, F., Bamba, O., 2016. Geochemistry, mineralogy, and isotope composition of Pb, Zn, and Cu in primary ores, gossan and barren ferruginous crust from the Perkoa base metal deposit, Burkina Faso. J. Geochem. Explor. 168, 49–64.
Li, X.H., Wang, J.Q., Chu, F.Y., Lei, J.J., Wang, H., Li, Z.G., 2018. Zn isotopes in hydrothermal sulfides and their oxidation products along the south mid-Atlantic ridge evidence of hydrothermal fluid deposition. Geo-Mar. Lett. 38 (2), 131–138.
Liao, S.L., Tao, C.H., Li, H.M., Barriga, F.J.A.S., Liang, J., Yang, W.F., Yu, J.Y., Zhu, C.W., 2018. Bulk geochemistry, sulfur isotope characteristics of the Yuhuang-1 hydrothermal field on the ultraslow-spreading Southwest Indian Ridge. Ore Geol. Rev. 96, 13–27.
Little, S.H., Vance, D., Walker-Brown, C., Landing, W.M., 2014. The oceanic mass balance of copper and zinc isotopes, investigated by analysis of their inputs, and outputs to ferromanganese oxide sediments. Geochim. Cosmochim. Acta 125 (1), 673–693.
Liu, S.A., Wu, H.C., Shen, S.Z., Jiang, G.Q., Zhang, S.H., Lv, Y.W., Zhang, H., Li, S.G., 2017. Zinc isotope evidence for intensive magmatism immediately before the end-Permian mass extinction. Geology 45 (4), 343–346.
Maréchal, C.N., Télouk, P., Albarède, F., 1999. Precise analysis of copper and zinc isotopic compositions by plasma-source mass spectrometry. Chem. Geol. 156 (1–4), 251–273.
Maréchal, C.N., Nicolas, E., Douchet, C., Albarède, F., 2000. Abundance of zinc isotopes as a marine biogeochemical tracer. Geochem. Geophys. Geosyst. 1 (5), 1929G–1999G.
Mason, T.F., Weiss, D.J., Horstwood, M., Parrish, R.R., Russell, S.S., Mullane, E., Coles, B.J., 2004. High-precision Cu and Zn isotope analysis by plasma source mass spectrometry part 2. Correcting for mass discrimination effects. J. Anal. At. Spectrom. 19 (2), 218–226.
Mason, T.F., Weiss, D.J., Chapman, J.B., Wilkinson, J.J., Tessalina, S.G., Spiro, B., Horstwood, M.S., Spratt, J., Coles, B.J., 2005. Zn and Cu isotopic variability in the Alexandrinka volcanic-hosted massive sulphide (VHMS) ore deposit, Urals, Russia. Chem. Geol. 221 (3), 170–187.
Metz, S., Trefry, J.H., 2000. Chemical and mineralogical influences on concentrations of trace metals in hydrothermal fluids. Geochim. Cosmochim. Acta 64 (13), 2267–2279.
Möller, K., 2012. Transition Metal Isotope Fractionation in Marine Hydrothermal Deposits of the Mohns Ridge, North Atlantic Ocean. University of Bergen, 2012.
Murowchick, J.B., Barnes, H.L., 1986. Marcasite precipitation from hydrothermal solutions. Geochim. Cosmochim. Acta 50 (12), 2615–2629.
Paradis, S., Jonasson, I.R., Lecheminant, G.M., Watkinson, D.H., 1988. Two zinc-rich chimneys from the plume site, southern Juan-De-Fuca ridge. Can. Mineral. 26 (3), 637–654.
Pasava, J., Tornos, F., Chrastny, V., 2014. Zinc and sulfur isotope variation in sphalerite from carbonate-hosted zinc deposits, Cantabria, Spain. Mineral. Deposita 49 (7), 797–807.
Petersen, S., Herzig, P.M., Hannington, M.D., 2000. Third dimension of a presently forming VMS deposit: TAG hydrothermal mound, Mid-Atlantic Ridge, 26 ° N. Mineral. Deposita 35 (2–3), 233–259.
Pichat, S., Douchet, C., Albarède, F., 2003. Zinc isotope variations in deep-sea carbonates from the eastern equatorial Pacific over the last 175 ka. Earth Planet. Sci. Lett. 210 (1–2), 167–178.
Qi, C.S., Zhu, X.K., Dai, M.H., Tang, S.H., Wu, M., Li, Z.H., Li, S.Z., Li, J., 2012. High-precision measurements of Fe and Zn isotopic ratios in marine sediments. Geochemica 41 (03), 197–206 (In Chinese with English abstract).
Reich, M., Deditius, A., Chryssoulis, S., Li, J.W., Ma, C.Q., Parada, M.A., Barra, F., Mittermayr, F., 2013. Pyrite as a record of hydrothermal fluid evolution in a porphyry copper system: a SIMS/EMPA trace element study. Geochim. Cosmochim. Acta 104 (1), 42–62.
Rosman, K.J.R., 1972. A survey of the isotopic and elemental abundance of zinc. Geochim. Cosmochim. Acta 36 (7), 801–819.
Sauter, D., Patriat, P., Rommevaux-Jestin, C., Cannat, M., Briais, A., 2001. The Southwest Indian Ridge between 49°15′E and 57°E: Focused accretion and magma redistribution. Earth Planet. Sci. Lett. 192 (3), 303–317.
Sauter, D., Cannat, M., Meyzen, C., Bezos, A., Patriat, P., Humler, E., Debayle, E., 2009. Propagation of a melting anomaly along the ultraslow Southwest Indian Ridge between 46°E and 52°20′E: Interaction with the Crozet hotspot? Geophys. J. Int. 179 (2), 687–699.
Schwartz, M.O., 2000. Cadmium in zinc deposits: economic geology of a polluting element. Int. Geol. Rev. 42 (5), 445–469.
Sun, Z.L., Li, J., Huang, W., Dong, H.L., Little, C.T.S., Li, J.W., 2015. Generation of hydrothermal Fe-Si oxyhydroxide deposit on the Southwest Indian Ridge and its implication for the origin of ancient banded iron formations. J. Geophys. Res. Biogeo. 120 (1), 187–203.
Tang, S.H., Zhu, X.K., Li, J., Yan, B., Li, S.Z., Li, Z.H., Wang, Y., Sun, J., 2016. New standard solutions for measurement of iron, copper and zinc isotopic compositions by multi-collector inductively coupled plasma-mass spectrometry. In: Rock and Mineral Analysis. 35(2). pp. 127–133 (In Chinese with English abstract).
Tao, C.H., Li, H.M., Huang, W., Han, X.Q., Wu, G.H., Su, X., Zhou, N., Lin, J., He, Y.H., Zhou, J.P., 2011. Mineralogical and geochemical features of sulfide chimneys from the 49°39′ E hydrothermal field on the Southwest Indian Ridge and their geological inferences. Chin. Sci. Bull. 56 (26), 2828–2838.
Tao, C.H., Lin, J., Guo, S.Q., John Chen, Y.S., Wu, G.H., Han, X.Q., German, C.R., Yoerger, D.R., Zhou, N., Li, H.M., Su, X., Zhu, J., 2012. First active hydrothermal vents on an ultraslow-spreading center: Southwest Indian Ridge. Geology 40 (1), 47–50.
Tao, C.H., Li, H.M., Jin, X.B., Zhou, J.P., Wu, T., He, Y.H., Deng, X.M., Gu, C.H., Zhang, G.Y., Liu, W.O., 2014. Seafloor hydrothermal activity and polymetallic sulfide exploration on the southwest Indian ridge. Chin. Sci. Bull. 59 (19), 2266–2276.
Tivey, M.K., Humphris, S.E., Thompson, G., Hannington, M.D., Rona, P.A., 1995. Deducing patterns of fluid-flow and mixing within the TAG active hydrothermal mound using mineralogical and geochemical data. J. Geophys. Res. Solid Earth 100 (B7), 12527–12555.
Toutain, J., Sonke, J., Munoz, M., Nonell, A., Polvé, M., Viers, J., Freydier, R., Sortino, F., Joron, J., Sumarti, S., 2008. Evidence for Zn isotopic fractionation at Merapi volcano. Chem. Geol. 253 (1–2), 74–82.
Wang, Y., Zhu, X.K., 2010. Application of Zn isotopes to study of mineral deposits: a review. Mineral Deposits 29 (05), 843–852 (In Chinese with English abstract).
Wang, Y., Sun, X.M., Wu, Z.W., Deng, X.G., Xu, L., Liang, Y.H., 2013. Preliminary study of Fe-Cu-zinc isotope characteristics of polymetallic sulfide in the ultraslow spreading Southwest Indian Ridge. Acta Mineral. Sin. S2, 665 (In Chinese with English abstract).
Wang, Y.J., Han, X.Q., Petersen, S., Frische, M., Qiu, Z.Y., Li, H.M., Li, H.L., Wu, Z.C., Cui, R.Y., 2017a. Mineralogy and trace element geochemistry of sulfide minerals from the Wocan Hydrothermal Field on the slow-spreading Carlsberg Ridge, Indian Ocean. Ore Geol. Rev. 84, 1–19.
Wang, Z.Z., Liu, S.A., Liu, J.G., Huang, J., Xiao, Y., Chu, Z.Y., Zhao, X.M., Tang, L.M., 2017b. Zinc isotope fractionation during mantle melting and constraints on the Zn isotope composition of Earth's upper mantle. Geochim. Cosmochim. Acta 198, 151–167.
Wang, D., Sun, X., Zheng, Y.Y., Wu, S., Xia, S.L., Chang, H.F., Yu, M., 2017c. Two pulses of mineralization and genesis of the Zhaxikang Sb–Pb–Zn–Ag deposit in southern Tibet: constraints from Fe–Zn isotopes. Ore Geol. Rev. 84, 347–363.
Wen, H.J., Zhu, C.W., Zhang, Y.X., Cloquet, C., Fan, H.F., Fu, S.H., 2016. Zn/Cd ratios and cadmium isotope evidence for the classification of lead-zinc deposits. Sci. Rep. 6 (25273).
White, W.M., 2014. Unconventional isotopes and approaches. In: Isotope Geochemistry. Wiley, pp. 327–384.
Wilkinson, J.J., Weiss, D.J., Mason, T.F.D., Coles, B.J., 2005. Zinc isotope variation in hydrothermal systems: preliminary evidence from the Irish Midlands ore field. Econ. Geol. 100 (3), 583–590.
Wu, Z.W., Sun, X.M., Wang, Y., Liang, Y.H., Xu, L., 2013. Preliminary study of Fe-Cu-zinc isotope characteristics of polymetallic sulfide in the Centrial Indian Ridge. Acta Mineral. Sin. S2, 672–673 (In Chinese with English abstract).
Yee, N., Phoenix, V.R., Konhauser, K.O., Benning, L.G., Ferris, F.G., 2003. The effect of cyanobacteria on silica precipitation at neutral pH: implications for bacterial silicification in geothermal hot springs. Chem. Geol. 199 (1–2), 83–90.
Zhang, J., Deng, J., Chen, H.Y., Yang, L.Q., Cooke, D., Danyushevsky, L., Gong, Q.J., 2014. LA-ICP-MS trace element analysis of pyrite from the Chang'an gold deposit, Sanjiang region, China: Implication for ore-forming process. Gondwana Res. 26 (2), 557–575.
Zhao, Y., Vance, D., Abouchami, W., de Baar, H.J.W., 2014. Biogeochemical cycling of zinc and its isotopes in the Southern Ocean. Geochim. Cosmochim. Acta 125, 653–672.
Zhou, J.X., Huang, Z.L., Lv, Z.C., Zhu, X.K., Gao, J.G., Mirnejad, H., 2014a. Geology, isotope geochemistry and ore genesis of the Shanshulin carbonate-hosted Pb–Zn deposit, southwest China. Ore Geol. Rev. 63, 209–225.
Zhou, J.X., Huang, Z.L., Zhou, M.F., Zhu, X.K., Muchez, P., 2014b. Zinc, sulfur and lead isotopic variations in carbonate-hosted Pb–Zn sulfide deposits, southwest China. Ore Geol. Rev. 58, 41–54.
Zhou, J.X., Luo, K., Li, B., Huang, Z.L., Yan, Z.F., 2016. Geological and isotopic constraints on the origin of the Anle carbonate-hosted Zn–Pb deposit in northwestern Yunnan Province, SW China. Ore Geol. Rev. 74, 88–100.
Zhu, Z.Y., Jiang, S.Y., Yang, T., Wei, H.Z., 2015. Improvements in Cu–Zn isotope analysis with MC-ICP-MS: a revisit of chemical purification, mass spectrometry measurement and mechanism of Cu/Zn mass bias decoupling effect. Int. J. Mass Spectrom. 393, 34–40.
Zhu, C.W., Wen, H.J., Zhang, Y.X., Fan, H.F., 2016. Cadmium and sulfur isotopic compositions of the Tianbaoshan Zn–Pb–Cd deposit, Sichuan Province, China. Ore Geol. Rev. 76, 152–162.
Zhu, C.W., Liao, S.L., Wang, W., Zhang, Y.X., Yang, T., Fan, H.F., Wen, H.J., 2018. Variations in Zn and S isotope chemistry of sedimentary sphalerite, Wusihe Zn-Pb deposit, Sichuan Province, China. Ore Geol. Rev. 95, 639–648.